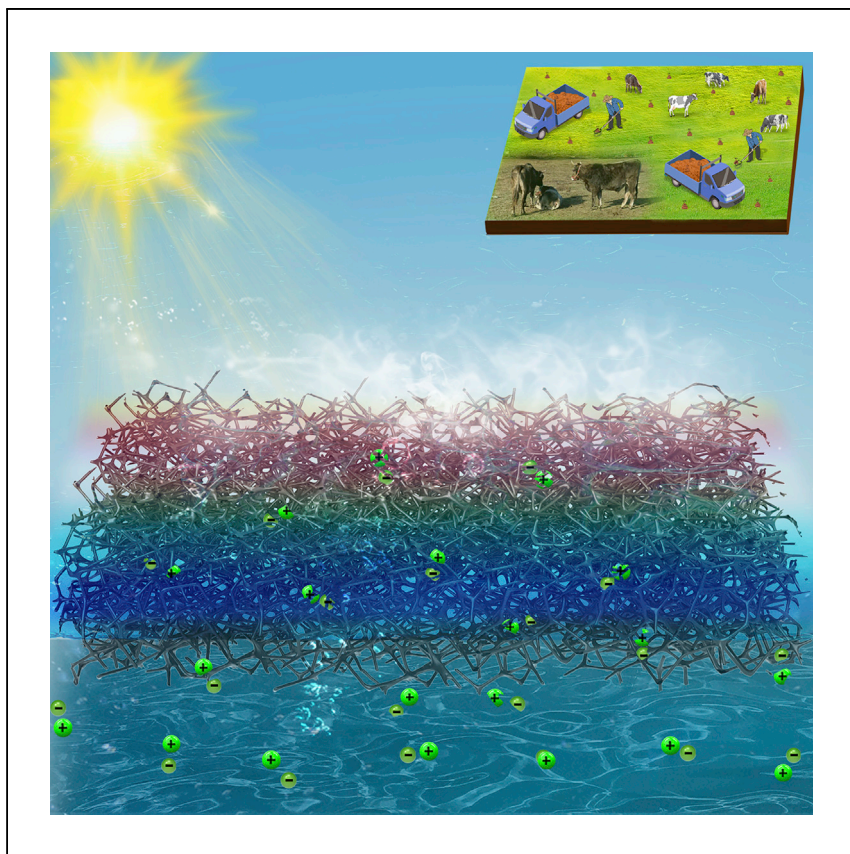## Article

Farm-waste-derived recyclable photothermal evaporator

A carbonized manure photothermal evaporator, derived from naturally abundant farm waste, is reported with high solar absorptance, effective water transportation, and rapid salt dissipation. It achieves high evaporation under 1-sun irradiance and shows potential for recyclable, durable, cost-effective, and energy-efficient solar-driven interfacial desalination.

Yanpei Tian, Xiaojie Liu, Jiansheng Li, ..., Yinsheng Wan, Gang Xiao, Yi Zheng

y.zheng@northeastern.edu

Highlights

A carbonized manure-derived fibrous foam for solar evaporation

Evaporation rate of $2.8 \, \text{kg} \, \text{m}^{-2} \, \text{h}^{-1}$ under 1 sun irradiance

Randomly aligned carbon fibers facilitating water and salt transportation

Stable operation in 15 wt% NaCl solution without salt accumulation

Article

Farm-waste-derived recyclable photothermal evaporator

Yanpei Tian,[1] Xiaojie Liu,[1] Jiansheng Li,[1] Yichen Deng,[1] Joseph A. DeGiorgis,[2,3] Shiyu Zhou,[4] Andrew Caratenuto,[1] Marilyn L. Minus,[1] Yinsheng Wan,[2] Gang Xiao,[4] and Yi Zheng[1,5,*]

SUMMARY

Interfacial solar steam generation is emerging as a promising technique for efficient desalination. Although increasing efforts have been made, challenges exist for achieving a balance among a plethora of performance indicators—for example, rapid evaporation, durability, low-cost deployment, and salt rejection. Here, we demonstrate that carbonized manure can convert 98% of sunlight into heat, and the strong capillarity of porous carbon fibers networks pumps sufficient water to evaporation interfaces. Salt diffusion within microchannels enables quick salt drainage to the bulk seawater to prevent salt accumulation. With these advantages, this biomass-derived evaporator is demonstrated to feature a high evaporation rate of 2.81 kg m^{-2} h^{-1} under 1 sun with broad robustness to acidity and alkalinity. These advantages, together with facial deployment, offer an approach for converting farm waste to energy with high efficiency and easy implementation, which is particularly well suited for developing regions.

INTRODUCTION

Increasing water pollution and groundwater exploitation are making clean water scarce.[1] One-fourth of people live in water-stressed regions with inadequate access to commercial water purification.[2] Generating water from seawater or sewage requires sophisticated engineering systems optimized in chemistry, physics, and materials science.[3,4] Serious impediments to sustainable water treatment range from energy consumption to expensive infrastructure installation and maintenance, exemplified by reverse osmosis systems[5] and multistage flash distillation,[6] establishing a barrier for sustainable water treatments.[7] At present, solar-driven distillation has drawn growing attraction because of its abundance, sustainability, and negligible carbon footprint.[8] Essential to any solar-driven water purification approach are metrics such as cost, efficiency, scalability, and water quality.

System efficiency can be improved by broad-spectrum sunlight trapping, enhanced photothermal conversion, dynamic water transport, heat localization, and salt rejection. Approaches range from selecting light-absorbing nanomaterials to metamaterials rich in macropores or honeycombs[9,10] and trapping light inside microstructures such as macropores.[11–13] One can also use superhydrophilic sponges to enable sufficient water transport to evaporation surfaces.[14,15] Solar-driven interfacial evaporation, localizing solar thermal energy within a confined region of the liquid-air interface as opposed to volumetric heating, can minimize thermal diffusion to the underlying bulk water. Artificially designed or naturally existing salt-rejection channels have been used to protect evaporators from salt accumulation, allowing for

[1]Department of Mechanical and Industrial Engineering, Northeastern University, Boston, MA 02115, USA

[2]Department of Biology, Providence College, Providence, RI 02918, USA

[3]Whitman Center, Marine Biological Laboratory, Woods Hole, MA 02543, USA

[4]Department of Physics, Brown University, Providence, RI 02912, USA

[5]Lead contact

*Correspondence: y.zheng@northeastern.edu

https://doi.org/10.1016/j.xcrp.2021.100549

continuous water desalination.[16,17] The above-mentioned design principles, high-absorptance solar absorbers, exceptional thermal localization, and optimized salt/water pathways have been demonstrated to approach the evaporation rate of the theoretical ceiling, 1.60 kg m^{-2} h^{-1} under 1 sun.[18,19] Hydrogel-based solar evaporators, which tune the interactions between water molecules and polymer networks and tailed surface wetting states, have been validated to achieve recording-breaking evaporation.[20] However, carbonized biomass, including wood,[21] sugarcane stems,[22] and mushrooms,[23] is a competitive materials candidate for a thermal evaporator.[24]

Recently, biomass-derived solar-driven water purification has received increasing attention. Taking advantage of the umbrella-shaped structure, Xu et al.[23] used calcined mushrooms as a solar evaporation device characterized by efficient water supply and vapor escape. He et al.[21] developed a bimodal porous balsawood-based salt-rejecting evaporator for high-salinity solar desalination. Fang et al.[25] substantiated another approach of using carbonized lotus seedpods rich in interconnected hierarchical pore structures for solar evaporation. Also worth noting, Geng et al.[26] developed a biowaste-based evaporator, using carbonized pomelo peels, whose microstructure is fractal in geometry. Those approaches are advantageous to wood-based evaporators that are burdened with a low evaporation rate and photothermal efficiency, owing to limited water transportation paths. However, one main deficiency in the mushroom and pomelo peel is that experiments were not based on saltwater, hence, they are not relevant to the problem of salt accumulation.

Manure, an organic matter chiefly consisting of water and cellulose, is an abundant biomass worldwide and is commonly used agriculturally as an organic fertilizer[27] or a biomass fuel precursor.[28] The randomly dispersed network of cellulose fibers forms percolated macropores inside the manure, offering a natural retention capacity of water. Inspired by the natural properties of manure, we propose carbonized manure (CM) as a material for efficient and sustainable photothermal evaporation, and we demonstrate a prototype that exhibits light trapping, rapid water pumping, and efficient salt rejection. The top diffused surface of CM features a solar absorptance of 0.98 due to light trapping enabled by multireflection inside the carbonized fibers. Strong capillarity as a result of the inherent superhydrophilicity pumps water rapidly to the evaporating interfaces. Heat localization of the poorly thermal conductive CM prevents the dissipation of heat downward to the water reservoir. These features yield an evaporation rate of 2.81 kg m^{-2} h^{-1} and a photothermal efficiency of 94.7% under 1 sun irradiance. Moreover, the microchannels efficiently prevent salt accumulation and ensure rapid salt drainage, which features an evaporation rate of 2.25 kg m^{-2} h^{-1} with high-salinity water (15 wt% NaCl). The fabricated CM evaporator prototype is robust against harsh environments with high acidity/alkalinity (pH, 1–13) or in boiling and ultrasonic water. After a long period of operation, the CM can be recalcined and recycled, becoming fresh after blending with additional fresh manure. The hemispherical CM structure is shown to yield an evaporation rate of 7.00 kg m^{-2} h^{-1}, providing another option for the 3 dimensional (3D) solar evaporation device. The CM evaporator has a vanishing raw materials cost and $1.32 m^{-2} electricity usage, making it competitive for large-scale implementation. The CM-based evaporator shows a promising way to achieve a balance between high evaporation rate, facial fabrication, cost-effectiveness, and easy deployment. The raw material for fabricating the CM photothermal evaporator is abundant availability and sustainability of raw material around the world, and the carbonization method is mature and relatively cost-effective for boosting the scalable deployment of solar desalination. Another key point of the CM photothermal evaporator is that it
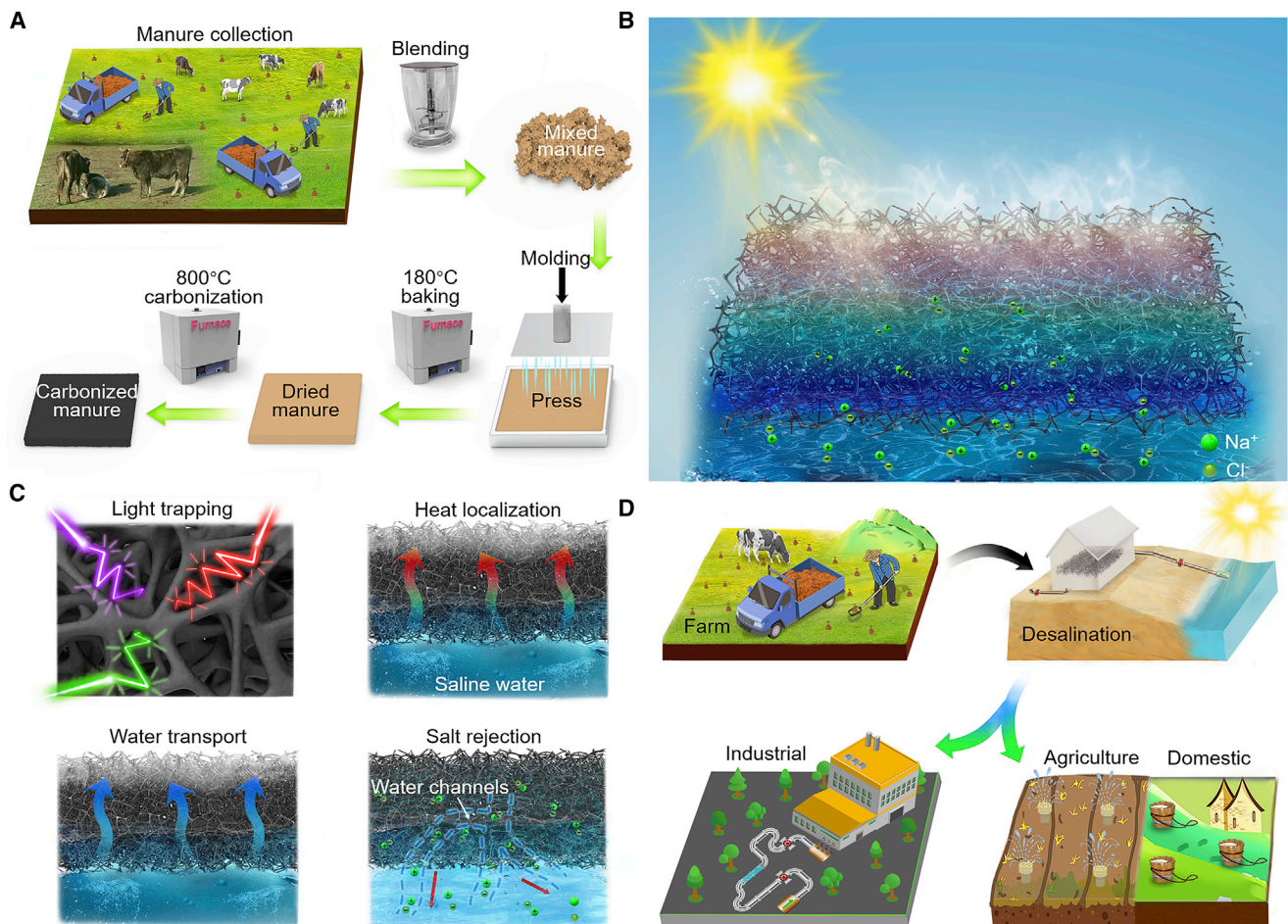
Figure 1. Concept of the manure-derived photothermal evaporator, fabrication methods, and the efficient solar desalination mechanism

(A) The fabrication process of the CM evaporator.

(B) Schematic elucidating the working mechanism of the CM solar evaporator: interconnected open microchannels serve as water transport channels that pump seawater, and the ultra-black CM surface functions as a photon-to-thermal layer to transform solar energy to heat.

(C) Schematic showing the light-absorption mechanism of the CM: the microchannels act as a "blackcavity," which traps the incident light (top left); (top right) low thermal conductivity of the microporous CM enables heat localization for a quick interfacial steam generation; (bottom left) randomly arranged black carbon fibers forming microchannels to pump the seawater; (bottom right) the salt dissipation is driven by the salt concentration gradient between the top and bottom regions of the CM evaporator.

(D) Schematic illustrations of the CM evaporator integrated into people's lives, which is scalable for industrial productions. The CM evaporator can be used for large-scale solar desalination and solar water treatment for industrial, agricultural, and people's lives.

can be recycled and becomes a functional material if mixed with additional fresh manure, while contributing to the development of a sustainable society. Therefore, we have demonstrated a promising pathway of using biowaste for scalable water generation, and the transform from farm waste to energy boosts the development of a sustainable society.

RESULTS AND DISCUSSION

Fabrication and working mechanism of the CM

We fabricated the manure-based evaporator in five steps: collecting, blending, molding, baking, and calcining. The blending step turns large manure chunks into smaller pieces and uses them for molding into a bulk form (e.g., a slab). After baking to dehydrate the manure, the carbonization process transforms the dried manure into porous CM latent with a high specific surface area (Figures 1A and S1). This

dramatically enhances the light absorption of the CM, as illustrated in Figure 1B. Seawater is pumped capillarily to the top evaporation surface and is heated interfacially by the localized thermal energy, converted from the trapped sunlight by the coarse black CM. The salt is drained to the microchannels due to ion concentration gradients between the evaporation interface and microchannel arrays. Heat is localized within the small volume beneath the evaporation interface, preventing thermal diffusion to the bulk water. Figure 1C elaborates these principles. The top CM surface is effective in light absorption as a result of trapped incident sunlight undergoing multiple reflections and interactions with matter (see Figure 1C, top left). The photothermal energy is primarily confined near the very top evaporation layers, which are poorly thermal conductive (see Figure 1C, top right). Strong capillary tensile force due to the superhydrophilic carbon fibers transports water flow to the upper interfacial evaporation layers, where continuous evaporation ensures the dynamic water supply (Figure 1C, bottom left). The ion concentrations in the upper region are higher than those in the lower region. The salt exchange within microchannels driven by the salt concentration difference continuously transports excess salt away from the evaporation regions (Figure 1C, bottom right). This prevents blockage of the water pathway and avoids undesirable sunlight reflections resulting from accumulated salt. To summarize, light absorption, interfacial evaporation, water pumping, and salt drainage work in concert to ensure uninterrupted interfacial evaporation and desalination. Figure 1D schematically illustrates the concept of how the manure-derived photothermal evaporator benefits human, industrial, and agricultural activities. This process manifests the principles of sustainable development by converting biowaste materials into functional materials.

Materials characterizations of the CM

Dried manure shrinks in dimensions after carbonization under an Ar protection environment (Figure 2A) and is mechanically stable (Figure S2), withstanding >330 times its weight without deformation. As shown in Figure 2B, we used Fourier transform infrared (FTIR) spectroscopy to identify the optimized carbonization temperature. At 800°C, the O–H stretching vibrations at ~3,500 cm^{-1} disappear. The decreasing peak intensity for the C–H bond at 2,920 cm^{-1} and the C=O bond at 1,645 cm^{-1} demonstrate the removal of cellulose/hemicellulose above 600°C. The –C=C– bond contributes to the light absorption after full carbonization. Conclusively, the optimized carbonization temperature is fixed at 800°C. As shown in Figure 2C, the X-ray diffraction pattern has a broad peak (circled in red, in 20°–25°) from the raw manure, which vanishes in CM treated at 800°C because of the carbonization of cellulose into carbon. The broad-spectrum absorption of CM is demonstrated by the solar absorptance spectra of dried CM and water-soaked CM, as shown in Figures 2D and S3. They show a solar absorptance of 0.98 across the solar wavelengths. This makes CM a nearly perfect solar absorber for harvesting solar energy. In contrast, the non-carbonized dried and soaked manure has a low solar absorptance of 0.77 and 0.86, respectively (Figures 2D and S3). The solar absorptance of the CM approaches unity, attributed to the light trapping of carbonized fibers despite different carbonization temperatures (Figure S4). The porous structures of the CM evaporator elongate the optical path to enhance the solar absorptance. The incident sunlight is barely reflected due to the nanoscale light trapping after multireflection and scatteration of the carbon fiber networks. The large difference in solar absorptance between uncarbonized manure and CM is mainly attributed to the high extinction coefficient of carbon compared with the negligible extinction coefficient of cellulose. Moreover, the solar absorptance is enhanced by scattering effects when carbon fibers are at the nanoscopic length scale. Furthermore, the solar absorptance of either dried or soaked CM is angle independent even at a high oblique angle
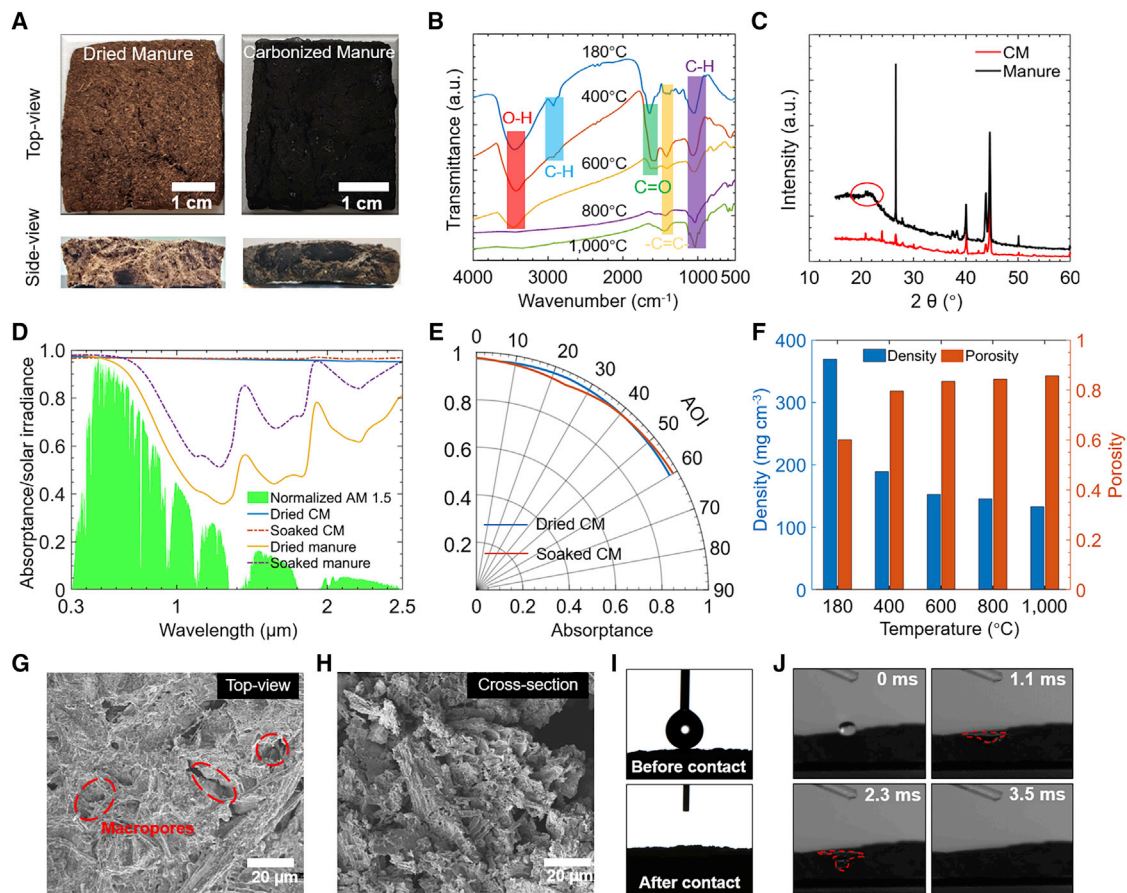
Figure 2. Mechanical robustness, optical properties, and thermal conductivity characterization of the CM

(A) Photographs of the dried manure (left) and CM (right).

(B) FTIR and XRD (C) spectra of the dried manure and CM carbonized at various temperatures. The red circled area represents the spectral peak of cellulose.

(D) The absorptance spectrum of the CM is exhibited against the AM 1.5 solar irradiance (ASTM G173).

(E) The average solar absorptance spectra for the CM across various angles of incidence (AOI).

(F) Density and porosity of the 180°C dried manure and CM carbonized at different temperatures.

(G and H) SEM images showing the (G) top view and (H) side view of the CM.

(I) Dynamic contact angle measurement of the CM.

(J) Rapid water absorption of the CM under a high-speed camera.

(60°), indicating that it can efficiently absorb sunlight from all angles of incidence (Figure 2E). This makes CM a promising photothermal absorber at any time of the day and any location on the Earth, rendering expensive solar tracking systems unnecessary. The porosity of the CM increases with elevated calcined temperatures, while its density decreases (Figure 2F). In this case, more air macropores are introduced, leading to its low thermal conductivity of 0.09 W m^{-1} K^{-1} and 0.15 W m^{-1} K^{-1} for CM and soaked CM, respectively (Figure S5). This protects the absorbed heat from diffusing downward to the bulk water and localizes heat to the small interfacial evaporation region, thereby increasing evaporator photothermal efficiency. Compared to a carbonized wood (CW)-based evaporator consisting of balsawood (Figures S5 and S6), CM has lower thermal conductivity than CW both with and without being water soaked. Top views and cross-sections of scanning electron microscopy (SEM) morphology for the manure carbonized at 800°C is shown in Figures 2G and 2H, and the carbon fiber size distribution is shown in Figure S7. The macropores facilitate light trapping by increasing the reflections and scattering inside the
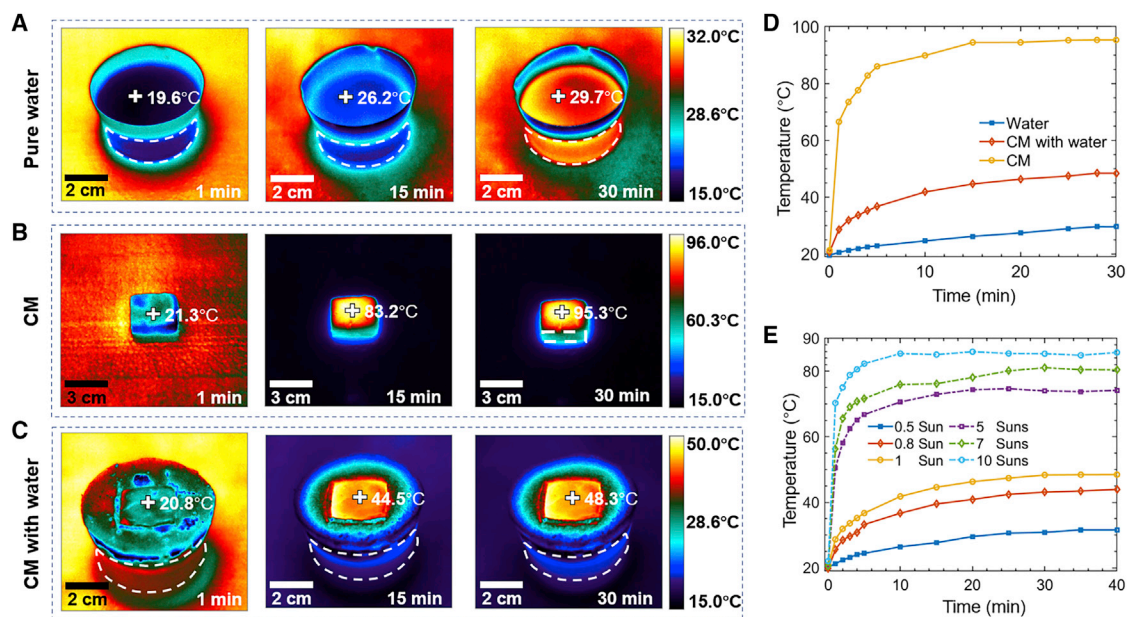
Figure 3. Photothermal response of the CM evaporator under an IR thermal camera

(A–C) IR images displaying the temperature distributions of the pure water, dried CM, and CM with adequate water supply from a cotton wipe under 1 sun irradiance after 1, 15, and 30 min. The white cross points to the same location of CM.

(D and E) Continuous temperature variations of the pure water, dried CM, and CM with adequate water supply from a cotton wipe under 1 sun (D) and various suns (E) irradiance.

pores (Figure S7), enabling a solar absorptance approaching unity. These pores also enhance the vapor escape. The cross-section of the CM shows water transport and salt-rejection channels formed by the cellulose fibers (Figure 2H), facilitating continuously efficient evaporation. The water absorption ratio curve is shown in Figure S5, elucidating the exceptional water-absorption capacity of CM as compared to CW. The water absorption ratio of CM reaches 4.5 g g^{-1}, which is 2 times that of the CW. The dynamic contact measurement also illustrates a water absorption ability, since the waterdrop disappears instantly after contact with the surface of the CM (Figure 2I). The rapid water absorption of CM is also demonstrated by the high-speed images shown in Figure 2J. The waterdrop stands only 1.1 ms after it falls on the CM surface and is soaked completely by the CM within 3.5 s. The mechanical robustness, broadband solar absorption, good heat localization, and rapid water absorption capability collaboratively render the CM a perfect evaporator for solar steam generation and desalination.

Photothermal response of the CM foam

The optothermal response of the CM is investigated with an IR camera. Figures 3A–3C shows the temperature distributions of the pure water, the dried CM, and the CM with sufficient water supply under 1 sun irradiance. The surface temperature of the dried CM rises rapidly to 83.2°C in the first 15 min and then stabilizes at 95.3°C after 30 min, demonstrating its fast optothermal response. For the CM with a sufficient water supply, its temperature quickly goes up to 44.5°C and reaches a final stable temperature of 48.3°C. The fast photothermal capability shortens the warmup time of the evaporation systems. The regions with the highest temperatures are confined in the very top surface of the CM in Figure 3B, and the average temperature of water increases from 27.8°C to 32.5°C, with a difference of the only 4.7°C from 1 to 30 min in Figure 3C. However, the pure water temperature rises from 19.6°C to

29.9°C, with a difference of 10.3°C (Figure 3A), which proves that heat is localized on the top evaporation regions of the CM. The homogeneous temperature distribution of the pure water is in contrast with the confined high-temperature region only on the top of the CM evaporator, demonstrating the heat localization capability of the CM evaporator. The side view of the CM evaporator with the water supply shows that the high-temperature region of CM evaporator is confined at the very top layer (Figure S8). For real outdoor applications, a rapid photothermal response and heat localization will dramatically boost the daily clean water yield. We further investigate the temperature evolutions of the CM evaporator with a sufficient water supply under various solar intensities, as shown in Figures 3D and 3E. The stagnation temperature of the CM evaporator surface reaches up to 87°C under the illumination of 10 suns, which is high enough to quickly evaporate water. Steam is seen when the CM evaporator is irradiated by 5 suns, and it still yields a stagnation temperature of 31.6°C under weak solar irradiance (0.5 kW m^{-2}), indicating its potential for working under sunlight after the sunrise and before the sunset.

Solar-driven steam-generation performance of the CM foam

The solar-driven evaporation rate of our CM evaporator is characterized by monitoring the mass difference of water in a plastic container (Figures 4A and 4B). The various solar intensities are realized by changing the optical concentration factors. The room temperature is ~21.3°C and the relative humidity fluctuates at ~35%. The dimensions of the CM are fixed at 28 mm × 30 mm × 5 mm, and its sides are surrounded by polyethylene foam to simultaneously prevent the vapor escaping from the sides and to localize heat to the CM evaporator. The CM is put on a layer of cotton wipes with a thickness of 0.5 mm, and another end of the cotton wipes is soaked within the bulk water through a slit on the polyvinyl chloride (PVC) foam. The PVC foam holds the CM and cotton wipes over the bulk water. The working mechanism of the evaporator is shown in Figure 4A. The broad-spectrum photothermal conversion and heat localization successfully converts and confines the solar thermal energy in the evaporation regions. The sufficient water absorption of the cotton wipes and CM continuously pump water to the top evaporation surfaces. Precipitated salt diffuses along the water transportation channels of CM and the cotton wipes downward into the bulk water. Figure 4B shows the quick steam generation of CM evaporator under 5 suns. The mass changes of pure water, CW evaporator, dried manure, and CM evaporator under 1 sun irradiance are elucidated in Figure 4C. The evaporation rate of the CM evaporator is 2.81 kg m^{-2} h^{-1}, which outperforms the dried manure- (1.44 kg m^{-2} h^{-1}) and CW- (1.97 kg m^{-2} h^{-1}) based evaporator and is 4.2 times that of the pure water (0.67 kg m^{-2} h^{-1}). A continuous test for 16 h yields an average evaporation rate of 2.73 kg m^{-2} h^{-1} and an average photothermal efficiency of 91.4% under 1 sun, evaluating the performance of long-time evaporation stability (Figure 4D). The evaporation capabilities of the CM evaporator under various solar illumination values are investigated (Figures 4E and S9). Enhanced solar intensities result in boosted evaporation rates, and the CM evaporator is demonstrated to have an evaporation rate of 20.45 kg m^{-2} h^{-1} under 20 suns. The evaporation rate under high concentration solar irradiance is below the linear estimated trends: the linear estimated evaporation rate should be 56 kg m^{-2} h^{-1}, while the measured result is 20.45 kg m^{-2} h^{-1} (Figure 4E). This discrepancy is due to the ultra-fast evaporation being larger than the water transport rate to the top evaporation surface. As discussed above, the evaporation rate of the CM evaporator (2.81 kg m^{-2} h^{-1}) is larger than the theoretical limit (1.60 kg m^{-2} h^{-1}, 1 kW m^{-2}). This mainly comes from the rough evaporation surface, resulting from the shrinkage of manure, which occurs during the high-temperature carbonization. This significantly expands the areas in which water evaporation takes place. To visualize the expanded areas of the CM surface, optical profilometry is applied to characterize the surface topography of CM, as shown in Figure 4F. The projection
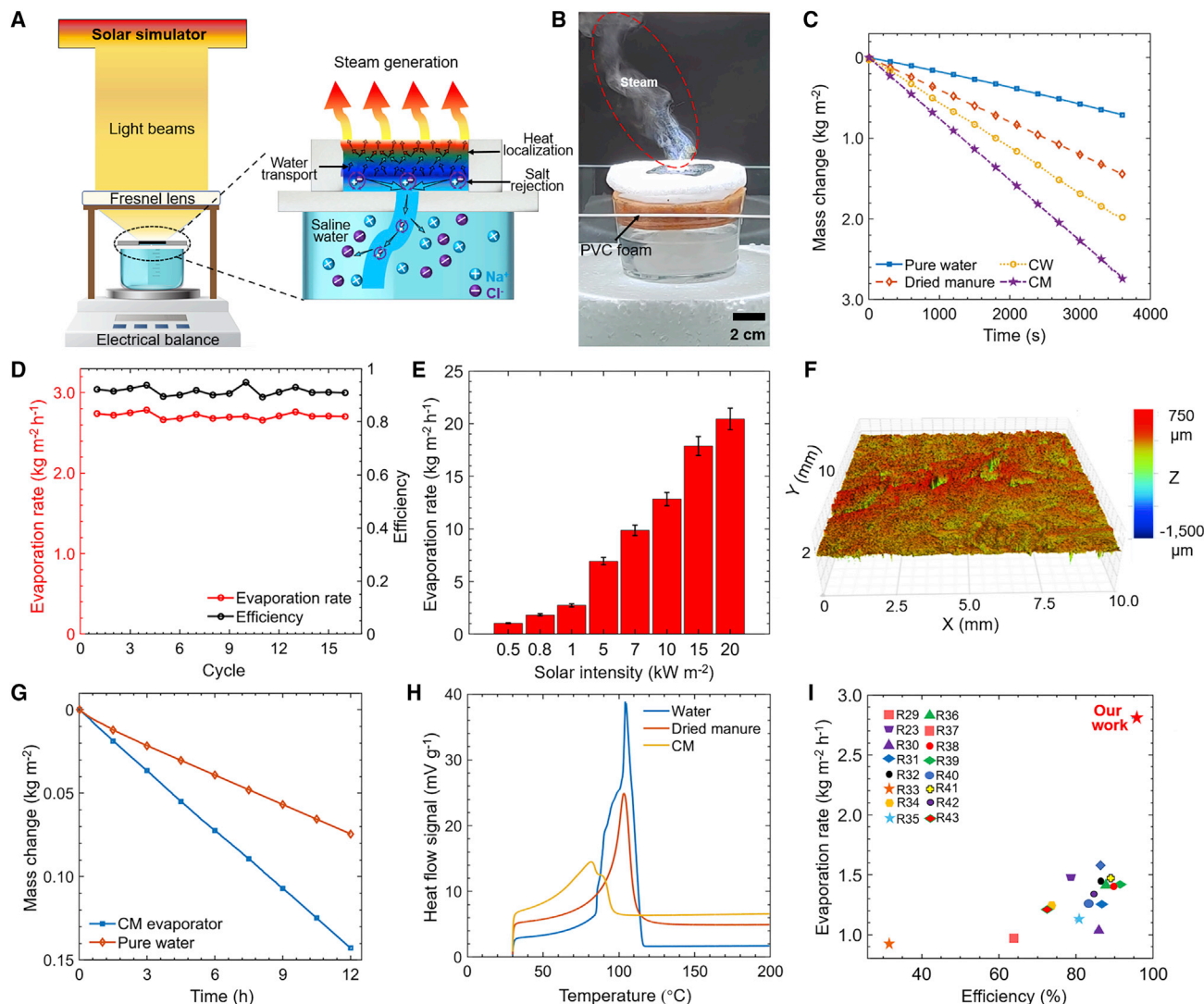
Figure 4. Experimental setup and the solar evaporation performance of CM evaporator

(A) Schematic illustrations of the experimental setup for solar steam generation.

(B) Photograph of the evaporator with visible vapor under 5 suns. The red circle shows the diffusion area of the generated steam.

(C) Mass changes of the pure water, dried manure, CW, and CM under a solar intensity of 1 kW m^{-2}.

(D) Evaporation rate and efficiency of the CM evaporator under 1 sun of long-time cycles.

(E) Evaporation rate evaluation of the CM evaporator under various solar intensities. Error bars represent the standard deviations of 3 repeated experimental results.

(F) The topography of the CM, indicating the increased evaporation area.

(G) Mass changes of the pure water and CM evaporator in the dark environment for 12 h.

(H) DSC thermograms of dried manure, CM, and pure water.

(I) The water evaporation rate and efficiency comparison between the CM evaporator and previously reported devices. Details are listed in Table S2.[23,29–43]

area of solar irradiation remains the same regardless of what the surface topography of the CM evaporator is. This effect is much like the 3D solar interfacial device that enhances the evaporation rate by increasing the evaporation area of the evaporator along the vertical direction. The average roughness of the CM surface is 71 μm, with a maximum peak height of 1,201 μm and a maximum valley depth of 1,666 μm (see Table S1 for details). The bumpy surface of the CM increases the evaporation area and thereby contributes to the rapid evaporation rate of the CM. To validate this, we evaluate the

evaporation of CM in a dark environment continuously for 12 h, eliminating sunlight effects, as shown in Figure 4G. The evaporation rate of the CM evaporator (0.142 kg m^{-2} h^{-1}) is 2.02 times that of pure water (0.07 kg m^{-2} h^{-1}) in a dark environment, which validates the idea that the evaporation area of the CM is larger than that of the pure water. The enhanced evaporation rate of CM is attributed to the expanded evaporation surface, as shown in the surface topographies measured by the optical profilometry since there are no components in CM with chemical groups of –OH, –NH$_2$, and –COOH that can activate water molecules. The enlarged evaporation surfaces can also be considered a reduced evaporation enthalpy of water, and the equivalent vaporization enthalpy of CM is 1,276 kJ kg^{-1} (see Note S1 for details), which is much smaller than the theoretical value (2,453.5 kJ kg^{-1} at 20°C). Differential scanning calorimetric (DSC) characterization shows the reduced evaporation enthalpy of water in CM. A sharp signal peak is observed at 100°C and then decreases dramatically, indicating that the water evaporates immediately and completely (Figure 4H). For the dried manure soaked with water, the heat flow signal peak is lower than that of the pure water, meaning that the dried manure has a large specific evaporation surface. The peaks of CM soaked with water are broader than those of pure water and dried manure. This demonstrates that the evaporation enthalpy of water in CM is reduced because the specific evaporation area of CM is expanded by the carbonization process. Figure 4I and Table S2 show a detailed comparison of evaporation rate and photothermal efficiency for the CM evaporator with other previously reported devices with 2D and 3D evaporator structures. It is worth noting that for a 2D photothermal evaporator, this means the evaporation surface (i.e., the surface for water vapor generating and escaping) spreads in x- and y-directions, while a 3D photothermal evaporator owns an evaporation surface in x-, y-, and z-directions. Regarding the CM photothermal evaporator proposed in this study, its evaporation surface during the experiments spreads only in the x- and y-directions, and we have also enclosed its sidewall using the polyethylene foam to prevent vapor from escaping from the sidewall surfaces, as shown in Figure 4B. We recognize that almost all of the solar evaporators can be classified into the 3D structures if viewed from a microscopic perspective since top surfaces are not smooth while zooming in to nanoscale. Therefore, we consider our CM photothermal evaporator to be a 2D structure because it does not have an evaporation surface in the z-direction. Both the evaporation rate and photothermal efficiency of our CM evaporator top this collection of data. With the advantages of cost-effectiveness and scalable fabrication, our CM evaporator can easily be applied to large-scale applications, especially for underdeveloped areas when considering the abundant raw materials resources and straightforward fabrication process.

Solar desalination, salt-rejection, and recycling performance of the CM foam

Salt-rejection capabilities and robustness in harsh environments are essential for solar-driven desalination. Salt accumulated in the water channels severely hinders water pumping, subsequent salt drainage, and light absorption, which dramatically decreases the evaporation rate to as low as zero. It is therefore essential to limit salt accumulation by using evaporator materials with excellent salt-rejection capabilities, particularly for applications involving high-salinity solutions. No salt accumulation occurs even using the 15 wt% NaCl solutions under 1 kW m^{-2} irradiance during the experiment. The evaporation rate of the CM decreases from 2.81 kg m^{-2} h^{-1} for pure water to 2.25 kg m^{-2} h^{-1} for the 15 wt% NaCl solution (Figure 5A). An evaporation rate of 20 kg m^{-2} h^{-1} under 20 suns irradiation is demonstrated, while the top surface of CM evaporator shows no salt accumulation, indicating its robustness for working in high-salinity (15 wt% NaCl solution, Figure 5A) environments and under high solar intensities (20 kW m^{-2}, Figure 5B). An average photothermal efficiency of 89% is achieved for the continuous 16-h solar desalination experiment using the 3.5 wt% NaCl solution (Figure S10). Figure 5C shows SEM images of the top view and cross-section of the CM after working for 6 h under 10
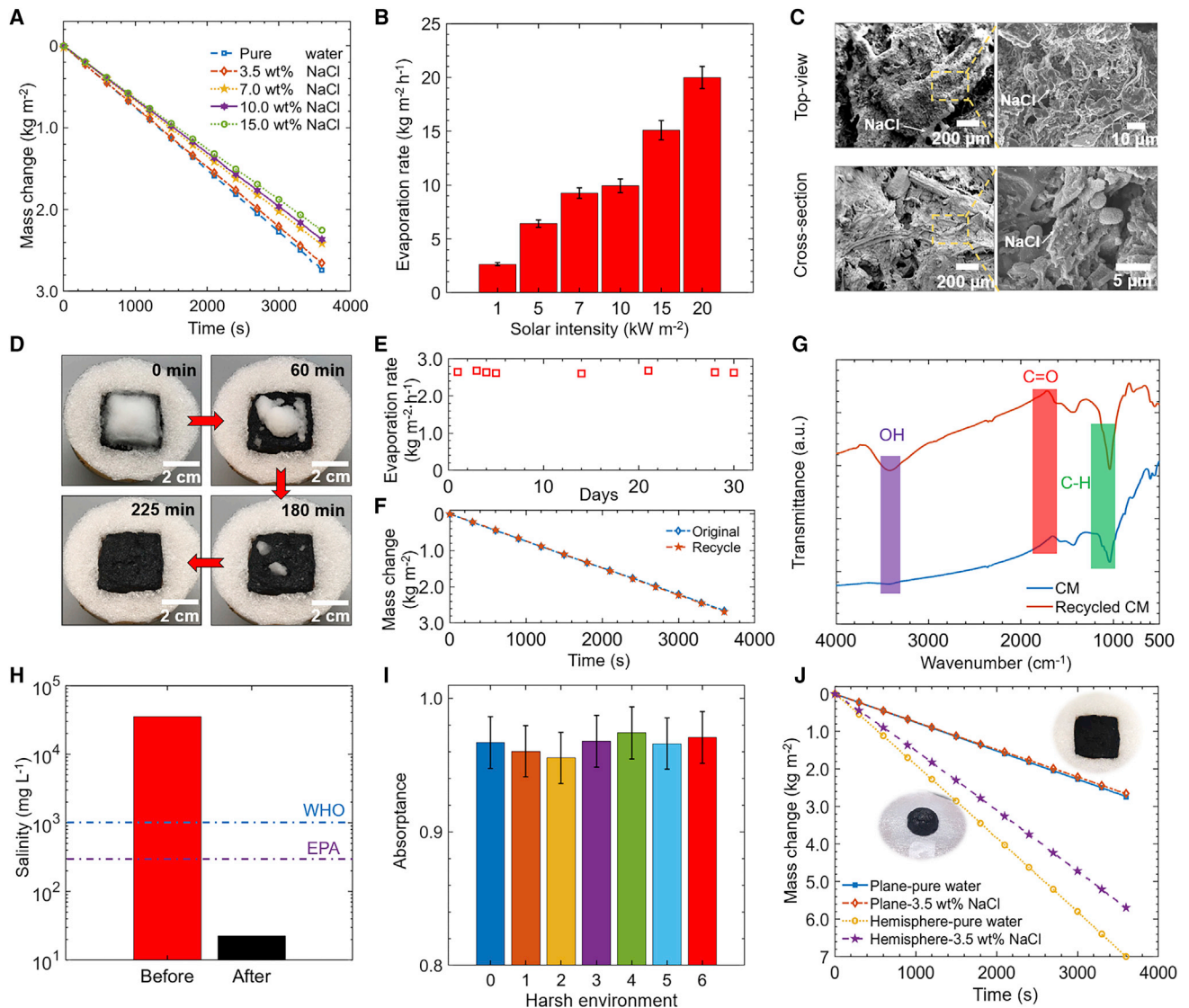
Figure 5. Desalination, salt-rejection, and recycling capabilities of the CM evaporator

(A) Mass changes of the CM evaporator in water of different salinities.

(B) Evaporation rates of the CM evaporator under solar irradiance of 1, 5, 7, 10, 10, and 15 kW m^{-2} with 3.5 wt% NaCl solution. Error bars represent the standard deviations of 3 repeated experimental results.

(C) The microscopic top view and cross-section for the CM evaporator under 10 suns for 6 h.

(D) Salt-rejection experiment using the 3.5 wt% NaCl solutions and 7 g NaCl showing the salt-dissipation functionality of the CM evaporator.

(E) Evaporation rates of the CM evaporator immersed in 15 wt% NaCl solution for a long time.

(F) Mass changes of the original CM evaporator and the recycled CM evaporator under 1 sun.

(G) FTIR spectra of the CM and recycled CM.

(H) The salinity comparison of the seawater before and after desalination.

(I) Average solar absorptance of the CM evaporator after treatment under various harsh environments: 0, original CM; 1, pH 1 solution for 24 h; 2, pH 13 solution for 24 h; 3, 95°C water for 2 h; 4, ultrasonic in water for 1 h; 5, immersed in 15 wt% NaCl solution for 14 days; and 6, working under a 10-kW m^{-2} solar irradiance for 6 h. Error bars represent the standard deviations of 3 repeated-measured results.

(J) Mass changes of a 2D flat CM evaporator and a 3D hemisphere CM evaporator with pure water and 3.5 wt% NaCl solutions, respectively.

suns in the 3.5 wt% NaCl solution. The salt crystallizes on the surface of the carbon fibers, but the water microchannels for water supply and salt rejection persist for continuous desalination. Time-lapse images of the salt-rejection experiment (Figure 5D) show that 7 g NaCl (average particle size: 10 μm in diameter) diffuses into the bulk NaCl

solution (3.5 wt%) within 3.75 h, validating the exceptional salt-drainage capability of CM. There is no salt accumulation on the top of the CM evaporator during the 16-h desalination experiments (Figure S11). The robust cycling performance of the CM evaporator in a high-salinity solution (15 wt% NaCl) is stable. By immersing the CM evaporator in a 15-wt% NaCl for certain days, such as 1, 3, 5, 7, 14, 21, 28, and 30 days, then taking it out for the evaporation rate tests using the 3.5 wt% NaCl solution each time. The CM evaporator yields an average evaporation rate of 2.65 kg m^{-2} h^{-1} (3.5 wt% NaCl solutions) for 28 days (with a total immersion time of CM = 720 h (Figure 5E). No degradation of the evaporation rate is observed. The recyclability of the evaporator is another key point for extending its lifetime for sustainable development. The mass changes of the original and recycled CM evaporator are nearly identical under 1 sun illumination, which validates the effectiveness of the recycled CM. The recyclability of CM indicates that the lifetime of the CM evaporator can be essentially infinite (Figure 5F). The FTIR transmittance spectra of the CM and the recycled CM also illustrate their consistency in spectra properties (Figure 5G), validating that the components of the evaporator do not change after being recycled. The absorption peak at ~3,400 cm^{-1} stems from the O–H stretching vibration, and peaks at 1,400–1,650 cm^{-1} come from the C=O and C=C bonds. The peak at 1,030 cm^{-1} results from the C–H deformation vibrations. To demonstrate the water quality after desalination, seawater collected from Revere Beach, near Boston, Massachusetts, is used to track the quality of produced water. After desalination, the salinity of purified water significantly decreases by 4 orders of magnitude, and it is 2 orders of magnitude below the freshwater standards defined by the World Health Organization (1‰) and the US Environmental Protection Agency (0.5‰) (Figure 5H). The overall solar absorptance, evaporation rate, and photothermal efficiency of the CM evaporator after treatments in various harsh environments are shown in Figures 5I and S12. These data demonstrate that the CM evaporator is also physically and chemically robust in the presence of acidic and alkaline solutions, high-temperature water (95°C), ultrasonic vibrations, long-time immersion in high-salinity water, and high illumination of 10 suns for 6 h. The evaporation rate of 3D evaporators with spatial structures has an outstanding performance that far exceeds the theoretical limit of the 2D structure due to the expanded evaporation area and the utilization of side areas that obtain energy from the ambient surroundings. To extend the application of the CM evaporator, a hemispherical CM evaporator is fabricated and characterized to show its excellent performance as a 3D structure. The hemispherical CM evaporator achieves an evaporation rate of 7.00 kg m^{-2} h^{-1} in the pure water and 5.70 kg m^{-2} h^{-1} in the 3.5 wt% NaCl solutions under 1 sun. The enhanced 3D structural CM evaporator shows promise for scalable implementations with low-cost deployment and easy fabrication methods.

We develop a cost-effective and eco-friendly solar thermal evaporator derived from carbonized manure. The system features an evaporation rate of 2.81 kg m^{-2} h^{-1} and a photothermal efficiency of 94.7% under 1 sun, outperforming most reported solar evaporators on a cost basis ($1.32 m^{-2} electricity usage and vanishing raw material cost). A hemispherical 3D spatial structure composed of CM yields a high evaporation rate of 7.00 kg m^{-2} h^{-1} with pure water and 5.70 kg m^{-2} h^{-1} with 3.5 wt% NaCl solutions under 1 sun. The porous CM microstructure enhances internal light scattering and multireflection, enabling effective light trapping and photothermal conversion. Microstructures of CM contribute to the low thermal conductivity and heat localization within the water evaporation interface. The interconnected microchannels and superhydrophilic carbonized fibers assist in fast capillary water transportation. Continuous clean water production in a high-salinity brine (15 wt%) is made possible by the effect of diffusion and convection inside channels that prevent salt accumulation. Furthermore, the chemical and physical robustness of the evaporator

makes it durable, and the simplicity in the fabrication process and material choices benefits large-scale and low-cost manufacturing. This biomass solar evaporator is attractive as an approach to generate clean water cost-effectively and efficiently from a wide variety of water sources, ranging from high-salinity brine to sewage.

EXPERIMENTAL PROCEDURES

Resource availability

Lead contact

Further information and requests for resources and reagents should be directed to and will be fulfilled by the lead contact, Yi Zheng (y.zheng@northeastern.edu).

Materials availability

This study did not generate new unique reagents.

Data and code availability

All data related to this study included in the article and Supplemental information will be provided by the lead contact upon reasonable request.

Materials

The cotton wipe used as the water path was supplied by Webril. The PVC insulation foam was purchased from McMaster-Carr. NaCl (99.0%) was supplied by Sigma-Aldrich. The fresh manure was collected from Blackbird Farm, Smithfield, RI, USA.

Sample preparations

The CM evaporator was fabricated as follows: the fresh manure was crushed into small pieces using a high-speed blender for 3 min and molded into a cuboid (5 cm × 5 cm × 0.5 cm). The manure cuboid was dried at 180°C for 20 min and carbonized in an Ar environment for 1 h. A 7-mm-thick PVC foam was cut into a circle with a diameter of 4.5 cm. The cotton wipes were cut into pieces with a dimension of 5 cm × 3 cm and soaked in the water through a slit in the PVC foam; then, the CM was placed on the cotton wipe. After using the CM photothermal evaporator for 15 h, we blended it with fresh manure using the blender and followed the molding and carbonization processes as listed above to fabricate a recycled CM photothermal evaporator. The hemispherical CM was fabricated by molding the fresh manure within a hemisphere and then followed by the carbonization process.

Solar desalination experiments

Solar desalination experiments were conducted under various solar fluxes using the solar simulator with a Fresnel lens to change the solar intensity. The mass of water was accurately monitored by an electrical scale (RADWAG, PS 1000) with a resolution of 0.001 g.

Materials characterization

The reflectance spectra (0.3–2.5 μm) were measured by a Jasco V770 spectrophotometer equipped with a Jasco ISN-923 integrating sphere. The incident angle of the light beam was fixed at an angle of 6°. The FTIR transmittance spectra were measured by a Jasco FTIR 6600. The reflectance spectra at different angles of incidence (AOI) were characterized by using wedges of different angles at the sample port of the Jasco V770 spectrophotometer.[44] The surface morphologies of samples were characterized by an acceleration voltage of 3 kV. The DSC thermograms were measured by a TA Instruments DSC Q200 with a heating rate of 5°C from 25°C to 200°C under an airflow flux of 50 mL min^{-1}. IR images of samples were taken using the FLIR A655C thermal camera at a resolution of 640 × 480 with a 25° lens. The

thermal conductivity of samples was characterized by the Hot Disk TPS 2500s. The contact angle was characterized by a SINDIN SDC-350 contact angle meter. The X-ray diffraction (XRD) spectra were characterized by the Bruker D8 X-ray Diffractometer, scanning from 15° to 100° with a step size of 0.02°. High-speed images were recorded by the Chronos 2.1-HD. The optical profilometry images were collected using a Bruker ContourGT-X8 optical profilometer. The solar intensity of the solar simulator was calibrated by the TES 132 solar power meter for each experiment under 0.5, 0.8, and 1 kW m^{-2}. For the experiments under 5, 7, 10, 15, and 20 kW m^{-2}, the solar intensity was calibrated by the OPHIR FL250A-BB35. The salinity of collected water samples was characterized by the Extech EC400 ExStik salinity meter. The pH value of the solutions was measured by the Dr.Meter pH-100 meter. Samples were imaged with a Zeiss Supra 40VP SEM after being coated with 10 nm platinum using a Leica MED 020 high-vacuum sputter coater.

SUPPLEMENTAL INFORMATION

ACKNOWLEDGMENTS

AUTHOR CONTRIBUTIONS

Conceptualization, Y.T., X.L., Y.W., G.X., and Y.Z. Investigation, Y.T., Y.D., J.D., S.Z., and A.C. Methodology, Y.T., J.L., Y.D., J.D., S.Z., A.C., M.M., Y.W., G.X., and Y.Z. Validation, Y.T., X.L., J.L., and M.M. Writing – original draft, Y.T. Writing – review & editing, A.C., G.X., and Y.Z. Supervision, funding acquisition, and project administration, Y.Z.

DECLARATION OF INTERESTS

The authors declare no competing interests.

REFERENCES

1. Guo, Y., Lu, H., Zhao, F., Zhou, X., Shi, W., and Yu, G. (2020). Biomass-derived hybrid hydrogel evaporators for cost-effective solar water purification. Adv. Mater. *32*, e1907061.

2. Ni, G., Zandavi, S.H., Javid, S.M., Boriskina, S.V., Cooper, T.A., and Chen, G. (2018). A salt-rejecting floating solar still for low-cost desalination. Energy Environ. Sci. *11*, 1510–1519.

3. Chen, G., Li, N., He, J., Qiao, L., Li, F., Wang, S., and Xu, X. (2020). Design of self-righting steam generators for solar-driven interfacial evaporation and self-powered water wave detection. J. Mater. Chem. A Mater. Energy Sustain. *8*, 24664–24674.

4. Chen, G., Li, N., He, J., Qiao, L., Li, F., Wang, S., Yu, L., Murto, P., Li, X., and Xu, X. (2019). Interfacial solar-to-heat conversion for desalination. Adv. Energy Mater. *9*, 1900310.

5. Malaeb, L., and Ayoub, G.M. (2011). Reverse osmosis technology for water treatment: state of the art review. Desalination *267*, 1–8.

6. Khawaji, A.D., Kutubkhanah, I.K., and Wie, J.M. (2008). Advances in seawater desalination technologies. Desalination *221*, 47–69.

7. Werber, J.R., Osuji, C.O., and Elimelech, M. (2016). Materials for next-generation desalination and water purification membranes. Nat. Rev. Mater. *1*, 1–15.

8. Zhu, L., Gao, M., Peh, C.K.N., and Ho, G.W. (2019). Recent progress in solar-driven interfacial water evaporation: advanced

designs and applications. Nano Energy 57, 507–518.

9. Wang, J., Li, Y., Deng, L., Wei, N., Weng, Y., Dong, S., Qi, D., Qiu, J., Chen, X., and Wu, T. (2017). High-performance photothermal conversion of narrow-bandgap ti2o3 nanoparticles. Adv. Mater. 29, 1603730.

10. Ito, Y., Tanabe, Y., Han, J., Fujita, T., Tanigaki, K., and Chen, M. (2015). Multifunctional porous graphene for high-efficiency steam generation by heat localization. Adv. Mater. 27, 4302–4307.

11. Ma, S., Qarony, W., Hossain, M.I., Yip, C.T., and Tsang, Y.H. (2019). Metal-organic framework derived porous carbon of light trapping structures for efficient solar steam generation. Sol. Energy Mater. Sol. Cells 196, 36–42.

12. Shi, L., Shi, Y., Zhuo, S., Zhang, C., Aldrees, Y., Aleid, S., and Wang, P. (2019). Multi-functional 3d honeycomb ceramic plate for clean water production by heterogeneous photo-fenton reaction and solar-driven water evaporation. Nano Energy 60, 222–230.

13. Hong, S., Shi, Y., Li, R., Zhang, C., Jin, Y., and Wang, P. (2018). Nature-inspired, 3d origami solar steam generator toward near full utilization of solar energy. ACS Appl. Mater. Interfaces 10, 28517–28524.

14. Zhang, P., Li, J., Lv, L., Zhao, Y., and Qu, L. (2017). Vertically aligned graphene sheets membrane for highly efficient solar thermal generation of clean water. ACS Nano 11, 5087–5093.

15. Zhang, P., Liao, Q., Zhang, T., Cheng, H., Huang, Y., Yang, C., Li, C., Jiang, L., and Qu, L. (2018). High throughput of clean water excluding ions, organic media, and bacteria from defect-abundant graphene aerogel under sunlight. Nano Energy 46, 415–422.

16. Zhang, W., Chen, X., Zhang, G., Li, J., Ji, Q., Hu, C., Ren, Z.J., Liu, H., and Qu, J. (2020). A salt-rejecting anisotropic structure for efficient solar desalination via heat–mass flux decoupling. J. Mater. Chem. A Mater. Energy Sustain. 8, 12089–12096.

17. Chen, J., Yin, J.L., Li, B., Ye, Z., Liu, D., Ding, D., Qian, F., Myung, N.V., Zhang, Q., and Yin, Y. (2020). Janus evaporators with self-recovering hydrophobicity for salt-rejecting interfacial solar desalination. ACS Nano 14, 17419–17427.

18. Zhou, L., Tan, Y., Wang, J., Xu, W., Yuan, Y., Cai, W., Zhu, S., and Zhu, J. (2016). 3d self-assembly of aluminium nanoparticles for plasmon-enhanced solar desalination. Nat. Photonics 10, 393–398.

19. Hu, X., Xu, W., Zhou, L., Tan, Y., Wang, Y., Zhu, S., and Zhu, J. (2017). Tailoring graphene oxide-based aerogels for efficient solar steam generation under one sun. Adv. Mater. 29, 1604031.

20. Guo, Y., Zhao, X., Zhao, F., Jiao, Z., Zhou, X., and Yu, G. (2020). Tailoring surface wetting states for ultrafast solar-driven water evaporation. Energy Environ. Sci. 13, 2087–2095.

21. He, S., Chen, C., Kuang, Y., Mi, R., Liu, Y., Pei, Y., Kong, W., Gan, W., Xie, H., Hitz, E., et al. (2019). Nature-inspired salt resistant bimodal porous solar evaporator for efficient and stable water desalination. Energy Environ. Sci. 12, 1558–1567.

22. Liu, J., Liu, Q., Ma, D., Yuan, Y., Yao, J., Zhang, W., Su, H., Su, Y., Gu, J., and Zhang, D. (2019). Simultaneously achieving thermal insulation and rapid water transport in sugarcane stems for efficient solar steam generation. J. Mater. Chem. A Mater. Energy Sustain. 7, 9034–9039.

23. Xu, N., Hu, X., Xu, W., Li, X., Zhou, L., Zhu, S., and Zhu, J. (2017). Mushrooms as efficient solar steam-generation devices. Adv. Mater. 29, 1606762.

24. Regan, P.M., and Kim, H. (2020). Water scarcity, climate adaptation, and armed conflict: insights from Africa. Reg. Environ. Change 20, 1–14.

25. Fang, J., Liu, J., Gu, J., Liu, Q., Zhang, W., Su, H., and Zhang, D. (2018). Hierarchical porous carbonized lotus seedpods for highly efficient solar steam generation. Chem. Mater. 30, 6217–6221.

26. Geng, Y., Sun, W., Ying, P., Zheng, Y., Ding, J., Sun, K., Li, L., and Li, M. (2020). Bioinspired fractal design of waste biomass-derived solar–thermal materials for highly efficient solar evaporation. Adv. Funct. Mater. 31, 2170020.

27. Mulbry, W., Westhead, E.K., Pizarro, C., and Sikora, L. (2005). Recycling of manure nutrients: use of algal biomass from dairy manure treatment as a slow release fertilizer. Bioresour. Technol. 96, 451–458.

28. Mekonnen, A., and Köhlin, G. (2008). Biomass fuel consumption and dung use as manure: evidence from rural households in the Amhara region of Ethiopia. https://media.rff.org/archive/files/sharepoint/WorkImages/Download/EfD-DP-08-17.pdf.

29. Chen, C., Li, Y., Song, J., Yang, Z., Kuang, Y., Hitz, E., Jia, C., Gong, A., Jiang, F., Zhu, J.Y., et al. (2017). Highly flexible and efficient solar steam generation device. Adv. Mater. 29, 1701756.

30. Zhu, M., Li, Y., Chen, F., Zhu, X., Dai, J., Li, Y., Yang, Z., Yan, X., Song, J., Wang, Y., et al. (2018). Plasmonic wood for high-efficiency solar steam generation. Adv. Energy Mater. 8, 1701028.

31. Li, Y., Gao, T., Yang, Z., Chen, C., Luo, W., Song, J., Hitz, E., Jia, C., Zhou, Y., Liu, B., et al. (2017). 3d-printed, all-in-one evaporator for high-efficiency solar steam generation under 1 sun illumination. Adv. Mater. 29, 1700981.

32. Zhu, M., Yu, J., Ma, C., Zhang, C., Wu, D., and Zhu, H. (2019). Carbonized daikon for high efficient solar steam generation. Sol. Energy Mater. Sol. Cells 191, 83–90.

33. Xue, G., Liu, K., Chen, Q., Yang, P., Li, J., Ding, T., Duan, J., Qi, B., and Zhou, J. (2017). Robust and low-cost flame-treated wood for high-performance solar steam generation. ACS Appl. Mater. Interfaces 9, 15052–15057.

34. Zhang, Z., Mu, P., He, J., Zhu, Z., Sun, H., Wei, H., Liang, W., and Li, A. (2019). Facile and scalable fabrication of surface-modified sponge for efficient solar steam generation. ChemSusChem 12, 426–433.

35. Li, T., Liu, H., Zhao, X., Chen, G., Dai, J., Pastel, G., Jia, C., Chen, C., Hitz, E., Siddhartha, D., et al. (2018). Scalable and highly efficient mesoporous wood-based solar steam generation device: localized heat, rapid water transport. Adv. Funct. Mater. 28, 1707134.

36. Mu, P., Zhang, Z., Bai, W., He, J., Sun, H., Zhu, Z., Liang, W., and Li, A. (2019). Superwetting monolithic hollow-carbon-nanotubes aerogels with hierarchically nanoporous structure for efficient solar steam generation. Adv. Energy Mater. 9, 1802158.

37. Wang, F., Wei, D., Li, Y., Chen, T., Mu, P., Sun, H., Zhu, Z., Liang, W., and Li, A. (2019). Chitosan/reduced graphene oxide-modified spacer fabric as a salt-resistant solar absorber for efficient solar steam generation. J. Mater. Chem. A Mater. Energy Sustain. 7, 18311–18317.

38. Zhao, X., Zha, X.J., Pu, J.H., Bai, L., Bao, R.Y., Liu, Z.Y., Yang, M.B., and Yang, W. (2019). Macroporous three-dimensional mxene architectures for highly efficient solar steam generation. J. Mater. Chem. A Mater. Energy Sustain. 7, 10446–10455.

39. Liu, C., Hong, K., Sun, X., Natan, A., Luan, P., Yang, Y., and Zhu, H. (2020). An 'antifouling' porous loofah sponge with internal microchannels as solar absorbers and water pumpers for thermal desalination. J. Mater. Chem. A Mater. Energy Sustain. 8, 12323–12333.

40. Lu, Y., Dai, T., Fan, D., Min, H., Ding, S., and Yang, X. (2020). Turning trash into treasure: pencil waste–derived materials for solar-powered water evaporation. Energy Technol. (Weinheim) 8, 2000567.

41. Zhang, J., Luo, X., Zhang, X., Xu, Y., Xu, H., Zuo, J., Liu, D., Cui, F., and Wang, W. (2021). Three-dimensional porous photo-thermal fiber felt with salt-resistant property for high efficient solar distillation. Chin. Chem. Lett. 32, 1442–1446.

42. Lu, Y., Wang, X., Fan, D., Yang, H., Xu, H., Min, H., and Yang, X. (2020). Biomass derived janus solar evaporator for synergic water evaporation and purification. Sustain. Mater. Technol. 25, e00180.

43. Dong, X., Si, Y., Chen, C., Ding, B., and Deng, H. (2021). Reed leaves inspired silica nanofibrous aerogels with parallel-arranged vessels for salt-resistant solar desalination. ACS Nano. https://doi.org/10.1021/acsnano.1c04035.

44. Tian, Y., Qian, L., Liu, X., Ghanekar, A., Liu, J., Thundat, T., Xiao, G., and Zheng, Y. (2021). High-temperature and abrasion-resistant metal-insulator-metal metamaterials. Mater. Today Energy 21, 100725.